Advanced Hybrid GaN/ZnO Nanoarchitectured Microtubes for Fluorescent Micromotors Driven by UV Light

Niklas Wolff, Vladimir Ciobanu, Mihail Enachi, Marius Kamp, Tudor Braniste, Viola Duppel, Sindu Shree, Simion Raevschi, Mariana Medina-Sánchez, Rainer Adelung, Oliver G. Schmidt, Lorenz Kienle,* and Ion Tiginyanu*

The development of functional microstructures with designed hierarchical and complex morphologies and large free active surfaces offers new potential for improvement of the pristine microstructures properties by the synergistic combination of microscopic as well as nanoscopic effects. In this contribution, dedicated methods of transmission electron microscopy (TEM) including tomography are used to characterize the complex hierarchically structured hybrid GaN/ZnO:Au microtubes containing a dense nanowire network on their interior. The presence of an epitaxially stabilized and chemically extremely stable ultrathin layer of ZnO on the inner wall of the produced GaN microtubes is evidenced. Gold nanoparticles initially trigger the catalytic growth of solid solution phase $(Ga_{1-x}Zn_x)(N_{1-x}O_x)$ nanowires into the interior space of the microtube, which are found to be terminated by AuGa-alloy nanodots coated in a shell of amorphous GaO_x species after the hydride vapor phase epitaxy process. The structural characterization suggests that this hierarchical design of GaN/ZnO microtubes could offer the potential to exhibit improved photocatalytic properties, which are initially demonstrated under UV light irradiation. As a proof of concept, the produced microtubes are used as photocatalytic micromotors in the presence of hydrogen peroxide solution with luminescent properties, which are appealing for future environmental applications and active matter fundamental studies.

1. Introduction

In the past, intensive research has been performed in the field of photocatalytic materials, predominantly covered by oxides such as TiO_2 and ZnO, oxynitrides or sulfides. These are engineered as single or multiple component nanostructures with potential applications ranging from photoreduction of CO_2, H_2 generation, self-cleaning surfaces, and artificial leaves.[1]

Future trends point to more complex nanoarchitectures by tuning the size, shape, and composition to achieve hierarchically structured nanocomposite photocatalytic semiconductor units.[1]

The fabrication of hollow particles and tubular structures with complex morphologies via template-assisted methods has been demonstrated to come up with exceptional properties for electrochemical energy application.[2] Template-based methods designed toward hollow structures provide high design flexibility and

N. Wolff, M. Kamp, Prof. L. Kienle
Synthesis and Real Structure
Institute for Materials Science
Kiel University
Kaiserstraße 2, 24143 Kiel, Germany
E-mail: lk@tf.uni-kiel.de
V. Ciobanu, Dr. M. Enachi, Dr. T. Braniste, Prof. I. Tiginyanu
National Center for Materials Study and Testing
Technical University of Moldova
Stefan cel Mare 168, Chisinau 2004, Moldova
E-mail: ion.tighineanu@cnstm.utm.md
V. Duppel
Nanochemistry
Max Planck Institute for Solid State Research
Heisenbergstraße 1, 70569 Stuttgart, Germany

Dr. S. Shree, Prof. R. Adelung
Functional Nanomaterials
Institute for Materials Science
Kiel University
Kaiserstraße 2, 24143 Kiel, Germany
Dr. S. Raevschi
Department of Physics and Engineering
State University of Moldova
Alexei Mateevici Str. 60, Chisinau 2009, Moldova
Dr. M. Medina-Sánchez, Prof. O. G. Schmidt
Institute for Integrative Nanosciences (IIN)
Leibniz IFW Dresden
Helmholtzstraße 20, 01069 Dresden, Germany
Prof. O. G. Schmidt
Material Systems for Nanoelectronics
Chemnitz University of Technology
Reichenhainer Straße 70, 09107 Chemnitz, Germany
Prof. I. Tiginyanu
Academy of Sciences of Moldova
Stefan cel Mare av. 1, Chisinau 2001, Moldova

ADVANCED
SCIENCE NEWS
www.advancedsciencenews.com

NANO · MICRO
small
www.small-journal.com

control of the final product shape making it one of the most versatile approaches in nanomaterial synthesis.[3] Herein, the concept of "nano casting" is a rigid mechanism;[4] this is deriving a predetermined structure by filling up voids in a mold with the material of choice and subsequent removal of the mold achieving desirable structures even down to the nanometer scale. With this respect, hard templates offer relatively easy and controllable processes resulting in a negative replica of the templates.[5] Commonly, inorganic, ordered porous solids including zeolites,[6] ordered mesoporous structures from silica[5] and carbon,[7] and anodic alumina oxides[8] are used as hard templates and recently metal-organic frameworks[9] have been reviewed for the same application.

The "filling" step is either characterized by coating the outer surfaces followed by selective template removal or by introducing a precursor material inside a porous structure via electrodeposition, galvanic replacement or controllable chemical transformation.[10]

Recently, the coating of zinc oxide (ZnO) microstructures as sacrificial templates raised the interest of the material science community, as ZnO can be easily dissolved in both acid and alkaline solutions making it suitable for producing hollow micro- and nanostructures.[11] Based on this, a variety of hollow structures such as hollow-Si tetrapods,[12] aerographite,[13] tetrapodal self-entangled carbon nanotube tube networks[14] and hollow-GaN tetrapods[15,16] using hydride vapor phase epitaxy (HVPE) for the deposition of GaN have been generated.[17] In this specific, the ZnO template and GaN lattices only show a small in-plane mismatch of 1.9% allowing for strong epitaxy[18] and forming p/n heterojunctions demonstrated useful for optical applications such as UV photodetectors[19] or light emitting diodes.[20]

In this context, another important application of such materials is related to the development of light-driven micromotors having one or 2D structures with high surface to volume fraction.[21] Especially micromotors based on photocatalytic materials such as pure TiO_2 or TiO_2 decorated with Pt, Ag, Au nanodots, or based on microarrays of porous TiO_2 nanotubes have been investigated.[22] Furthermore, using atomic layer deposition, Dong et al.[23] fabricated hybrid ZnO–Pt tubular micromotors with light-enhanced propulsion based on strong photocatalytic properties of ZnO and chemical catalytic properties of Pt. These micromotors, however, did not exhibit on–off capabilities and their chemical stability over time remained undisclosed since ZnO is known to suffer from photocorrosion in an aqueous medium.

Recently, the versatile GaN has attracted interest especially due to its adaptable optical and electrical properties,[24,25] which were also exploited for photocatalysis, suggesting outstanding photocatalytic activity of GaN nanowires (NWs) superior to TiO_2 NWs and even ZnO NWs with chemical stability under harsh acidic conditions.[26] At the same time, GaN is a nontoxic, biocompatible material, which opens wide possibilities for medical applications.

Further radical improvement of GaN electrical, optical, and photocatalytic properties can be achieved by various approaches: tailoring the bandgap energy is possible by 1) the concentration x of co-doping with ZnO forming a solid solution $(Ga_{1-x}Zn_x)$ $(N_{1-x}O_x)$[27] or by 2) tailoring the NW facets by changing the morphology of the NWs from straight to zig-zag.[28] 3) The surface modification with a noble metal cocatalyst[29] demonstrated to improve the visible-light-driven degradation of an organic dye by the factor of 8 with respect to pristine $(Ga_{0.75}Zn_{0.25})$ $(N_{0.75}O_{0.25})$ enhancing the photocurrent response, which is usually associated with localized surface plasmon resonance.[30,31] 4) The reduction of the structure size is believed to further improve the photocatalytic performance.

Hence, the irradiation with designed light sources including wavelengths of the infrared, the visible or UV spectrum could be an efficient energy source for the purpose of achieving directional controlled motion in case of GaN or modified GaN:ZnO tubular microstructures functionalized with a noble metal cocatalyst. Indeed, many research groups focused their efforts on developing chemical micromotors[32] capable of converting, e.g., chemical fuels into self-propelled mechanical motion by catalytic reactions.[33–37] Here, light-driven photocatalytic micromotors[38–40] are one of the most studied due to their excellent propulsion properties. The most commonly known light-induced propulsion mechanisms can be classified into self-diffusiophoretic propulsion,[41] bubble propulsion,[42,43] and self-electrophoretic propulsion.[44]

Their strong propulsion, efficient direction control, and abundant functions hold great promise in a number of potential applications ranging from, e.g., cargo transportation in biomedicine[45–48] to environmental cleaning.[49–54]

However, with decreasing tube diameter, the fluid dynamics in confined volumes like capillaries can either inhibit bubble generation or block the liquid flow. In this context, the development of micromotors based on other propulsion mechanisms, e.g., diffusiophoretic motion, circumvents these issues.[22]

In this contribution, we discuss the synthesis, the morphology, chemical composition, and atomic structure of the hierarchical ordered micro-/nanostructure characterized by TEM analysis using scanning (S)TEM tomography, electron diffraction (ED), high-resolution HRTEM imaging, and energy-dispersive X-ray spectroscopy (EDS). Further, we demonstrate the fluorescent light-driven diffusiophoretic motion of the chemically stable and hierarchical nanostructured micromotors showing switchable on–off characteristics. These micromotors are based on hybrid GaN/ZnO microtubes, the outer surface favoring hydrophobicity and the inner hydrophilic surface being functionalized by solid-solution phase $(Ga_{1-x}Zn_x)$ $(N_{1-x}O_x)$ nanowires (NWs) terminated by cocatalytic AuGa-alloy nanodots.

2. Results and Discussion

2.1. Morphology, Composition, and Structure

Considering the recently demonstrated high chemical stability of ultrathin ZnO layers when interfacing GaN,[15] we propose a novel type of GaN/ZnO microtubes, decorated with Au nanodots. The elaborated technological route consists of the following steps as illustrated in **Figure 1**. First, gold nanodots are deposited by plasma sputtering on the surface of ZnO microneedles exhibiting a gradient of transverse size along their longitudinal axis. Second, the growth of a thin GaN layer
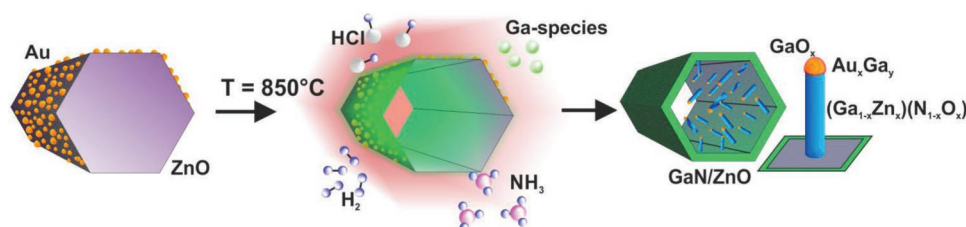
ADVANCED
SCIENCE NEWS
www.advancedsciencenews.com

NANO · MICRO
small
www.small-journal.com

Figure 1. Schematic representation of the synthetic route of GaN/ZnO nanoarchitectured microtubes with an ingrown solid-solution nanowire network. ZnO microwires covered with gold nanoparticles (left image) are subjected to a hydrothermal environment initiating epitaxial growth of GaN while simultaneously etching the ZnO (middle image). The final product of GaN microtubes with a thin ZnO layer chemically stabilized on the inside walls promoting the growth of a nanowire network (right image).

using HVPE is initiated. The process of GaN epitaxial growth is accompanied by the simultaneous hydrothermal removal of ZnO, normally with the exception of an ultrathin ZnO layer which remains at the interface.[15] In the final steps of this process, the Zn- and O-enriched gaseous environment inside the GaN microtubes propagates the growth of NW networks with solid solution phase $(Ga_{1-x}Zn_x)(N_{1-x}O_x)$ composition on the interior wall of the microtubes. The chemical reactions in confined conditions lead to the formation of AuGa-alloyed nanodots enveloped in a shell of amorphous gallium oxide (GaO_x).

The morphology of the ZnO microneedles serving as sacrificial templates and the resulting GaN/ZnO nanoarchitectured microtubes were investigated using a scanning electron microscope (SEM) (see **Figure 2**). The ZnO microneedles were produced with a modified flame transport synthesis[55] (FTS) and possess high aspect ratios of 300–1000 µm in length and ≈1–10 µm of micrometers in diameter (see Figure 2a,b). Uniformly distributed Au nanodots (10 nm) were observed along the microneedles (see Figure 2c). During the epitaxial growth of GaN accompanied by simultaneous ZnO removal, the microneedles are transformed into the GaN/ZnO microtubes with a hexagonal cross-section (see Figure 2d,e). The inner surface of these microtubes with a wall thickness in the ≈30 nm

range is decorated by NWs demonstrated to initially grow perpendicular to the {$\bar{1}100$} facets and show straight or kinked structures (see Figure 2f).

Scanning transmission electron microscopy (STEM) was performed to obtain more insights into the composition of different nanostructures on the inner surface of the conical microtubes (**Figure 3**). The template-directed hollow structures synthesized by HVPE produced microtubes and Au dot terminated NWs were observed at the microtubes inner surface (see Figure 3a,b).

Results of the electron diffraction (ED) experiments (Figure 3c) indicate that these GaN/ZnO microtubes grow as single crystals, showing c-axis directed growth of the Wurtzite-type structure. The high density of NWs grown inside the hollow microstructures was visualized by a 3D volume reconstruction computed from STEM tomography experiments (see Figure S1 and Movie S1 in the Supporting Information). For this, a sample was tilted over a large angular range along its longitudinal axis using a high angle tilt holder, and the acquired images were combined for a 3D reconstruction (see Figure 3d). A cross-sectional image of this reconstruction is presented with colored isosurfaces of the tube and NWs inside (Figure 3d). The examined GaN/ZnO microtube fragment exhibited a hexagonal
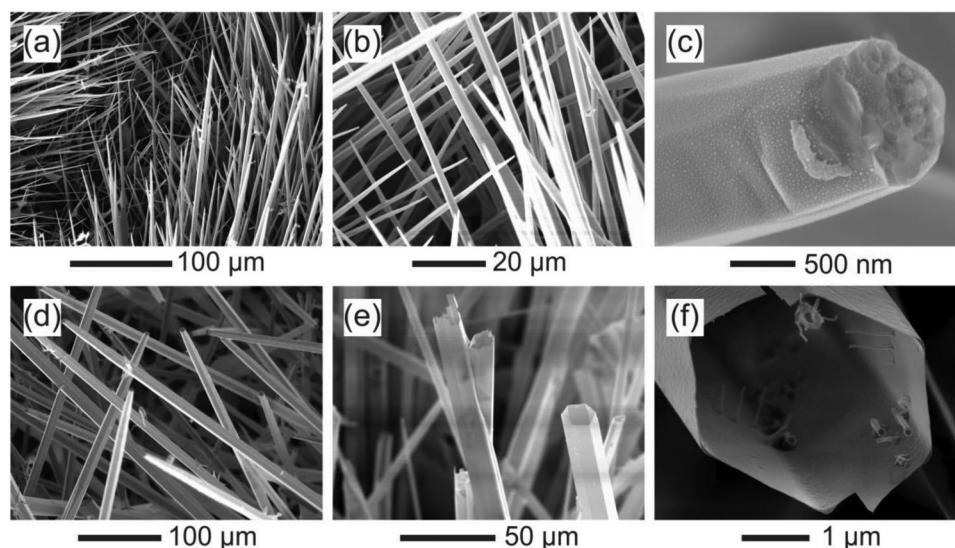

Figure 2. SEM micrographs of a,b) the initial hedgehog-like ZnO microneedles used as templates and c) Au nanodots deposited on ZnO microneedles, d–f) GaN/ZnO microtubes with ingrown NWs.
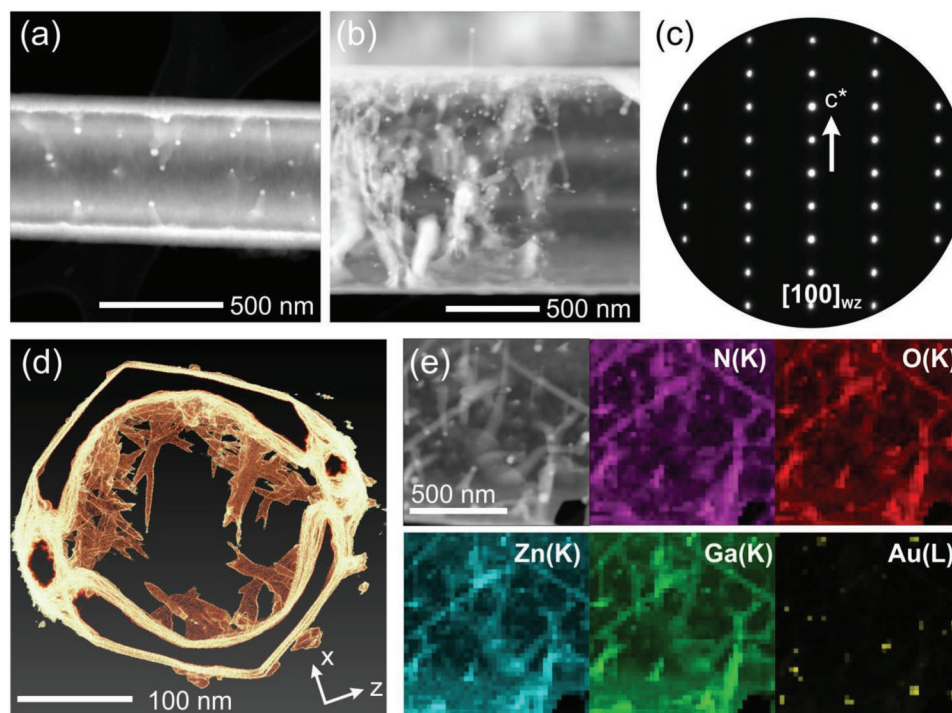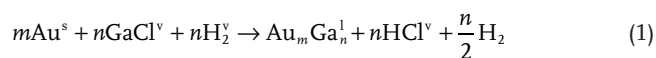
ADVANCED
SCIENCE NEWS
www.advancedsciencenews.com

NANO · MICRO
small
www.small-journal.com

Figure 3. a,b) Scanning TEM images of GaN/ZnO microtubes showing nanowire growth on the inner surface. c) SAED pattern obtained from a GaN/ZnO microtube confirming *c*-axis directed growth in a Wurtzite-type structure. d) Cross-section through the *x*–*z* plane of a 3D tomographic volume reconstruction. e) EDS elemental maps on a sliced microtube colored accordingly for ease of understanding.

cross-section with an outer diameter of ≈300 nm and uniform wall thickness (20–30 nm). The hexagonal shape appears not to be preserved on the inner wall surface. The reconstructed model showed buckled surfaces on the outside and interrupted surfaces on the inside in *z*-direction (*z* being the direction of the electron beam perpendicular to the rotation axis of the *x*–*y* plane), which is explained by a so-called computational missing wedge artifact in that particular direction.[56,57]

Elemental analysis of the characteristic X-rays emitted from a GaN/ZnO microtube fragment was performed via STEM EDS. The superimposed identical spatial distribution of Ga, Zn, N, and O (see Figure 3e) discloses an ultrathin residual layer of ZnO interfacing GaN. This confirms the stability of the ZnO/GaN interface as it was previously reported.[15] Nanowires terminated by Au nanodots were further imaged to propagate into the free space of the tube as visualized in **Figure 4**. In congruence to the SEM micrographs, the NWs shown in the TEM image of Figure 4a grow straight with tapered or needle-shaped morphology, whereas the NWs depicted in the STEM image of Figure 4b show kinks and uniform cylindrical morphology. Such morphological differences of VLS grown NWs are known to be induced by numerous variables in the system describing the static or dynamic local reaction conditions including temperature, the supply rate of reactive species and droplet physics of the catalyst of which an in-depth discussion is provided by Mohammad.[58] Hence, the uncontrolled reaction conditions during the HVPE process and hydrothermal dissolution of ZnO lead to the metal-catalytic VLS growth of NWs of different morphology according to the supposed following reaction schemes[59,60]

$$m\text{Au}^s + n\text{GaCl}^v + n\text{H}_2^v \rightarrow \text{Au}_m\text{Ga}_n^l + n\text{HCl}^v + \frac{n}{2}\text{H}_2 \quad (1)$$

$$\text{Au}_m\text{Ga}_n^l + n\text{NH}_3^v \rightarrow m\text{Au}^s + n\text{GaN}^s + 3n/2\text{H}_2 \quad (2)$$

However, in the Zn and O enriched hydrothermal environment inside the microtubes, the growth of a solid solution phase $(\text{Ga}_{1-x}\text{Zn}_x)(\text{N}_{1-x}\text{O}_x)$ is proposed by the EDS analysis on the NWs presented in Figure 4c. In this respect, the elemental distribution maps show the superimposed spatial distribution of X-ray excitations of Ga(K) and Zn(K) edges together with N and O signals.

Further, the EDS analysis proposes that the Au metal catalyst alloyed with Ga is forming intermetallic phases of the binary AuGa system,[61] the alloy being capsulated by a shell of GaO$_x$. Note that a careful evaluation of the X-ray distribution maps considers the partially overlap of the Zn(K) and Au(L) excitation energies ≈9.60 keV in order to reflect on possible misinterpretation on the signal intensity in the Zn(K) map displayed at the metal catalyst site. Further, the evaluation of the Zn(L) excitation (not shown) reveals partial overlap with Ga(L) excitation. Thus, no conclusive statement can be made on the spatial distribution of Zn at the metal site due to double interference events in the maps shown. However, EDS point measurements did not collect significant intensity of Zn(Kα), concluding that essentially no Zn or only a trace of Zn is alloyed into AuGa (see Figure S2 in the Supporting Information). Additionally, a conclusive statement about the nitrogen distribution has to be taken with care since the signal is smeared out by an increased background induced by the presence of carbon species.
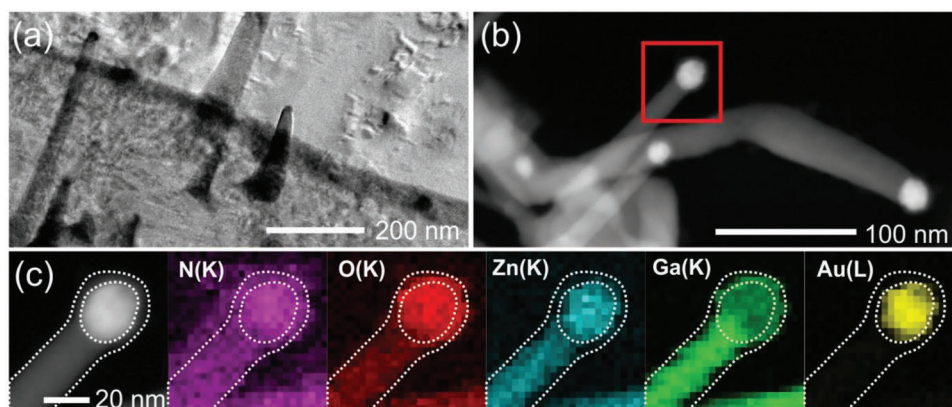
ADVANCED
SCIENCE NEWS
www.advancedsciencenews.com

NANO · MICRO
small
www.small-journal.com

Figure 4. a) TEM image and b) STEM image of NWs grown at the inner surface of the wall. c) STEM EDS elemental maps of metal terminated wires grown at the inner wall surface of GaN/ZnO microtubes. The elemental maps show the distribution of Ga, N, Zn, O, and Au as components of the metal terminated wires.

The averaged concentration of Zn in the solid solution NWs has been determined by numerous EDS point measurements performed on individual NWs. The calculated compositions of $x = 0.12 \pm 0.2$ are very close to single-phase solid solution NWs with $x \approx 0.12$ grown by Han from an Au nanocrystal via a VLS reaction process.[62]

The structure of the solid solution phase $(Ga_{1-x}Zn_x)(N_{1-x}O_x)$ NWs and alloy nanodots was investigated by high-resolution TEM and reciprocal space analysis using fast Fourier transformation (FFT) images and electron diffraction performed also in the precession mode (PED).[63] The real structure of the NWs is characterized by a high density of basal plane defects including polytypic intergrowth and polysynthetic twinning apparent from the TEM investigation shown in **Figure 5**. The structural details of polytypic Wurtzite (WZ) and Zincblende-type (ZB) intergrowth have been described, e.g., by Dick et al.[64] or Caroff et al.[65] For the description the relative positions of Ga- and N-atom $(001)_{WZ}$ bilayers are labeled as A, B, or C. The repetitive

hexagonal stacking sequence AB of $(001)_{WZ}$ closed packed planes in growth direction is frequently interrupted by the single or repetitive introduction of a misplaced bilayer C (see Figure 5a). Along the depicted nanostructure, this introduces cubic nanolamellae with single or multiple cubic ABC stacking sequences along $[111]_{ZB}$. The WZ and ZB components are illustrated by the red and blue colors in the high-resolution TEM micrograph associated with the electron diffraction pattern and FFTs given in Figure 5b. The WZ-type lamellae are oriented along $[100]_{WZ}$ and the ZB-type lamellae in $[110]_{ZB}$ zone axis orientation, respectively. The structural heterogeneity can alter the relative orientation of the WZ lamellae attached to both sides of a ZB lamella, particularly, in case of an odd number of layers inside the ZB lamella both WZ lamellae are mirrored to each other, i.e., their stacking sequence changes from AB to AC. More complicated examples of NWs featuring hexagonal-cubic intergrowths are depicted in Figure S3 (Supporting Information).
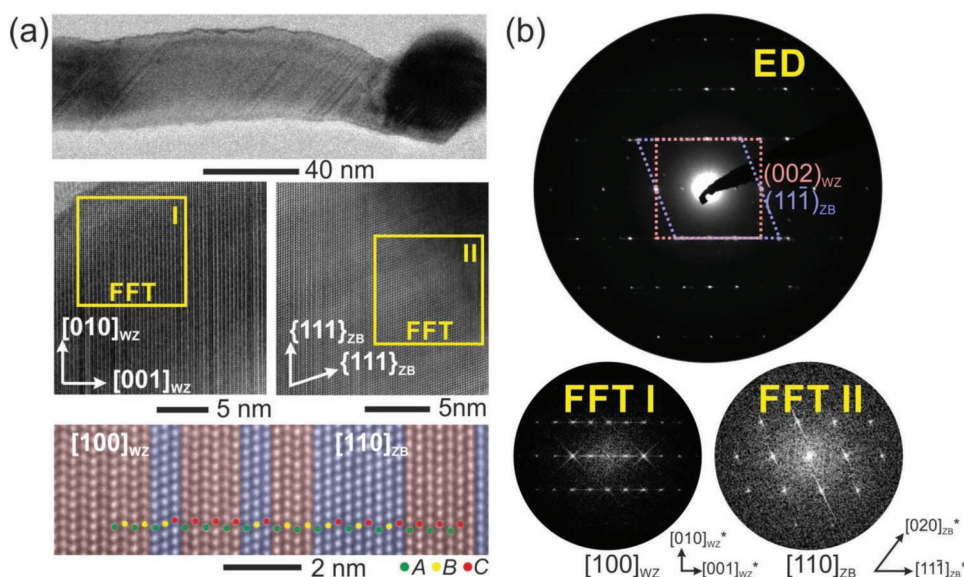

Figure 5. Crystallographic data of a representative $(Ga_{1-x}Zn_x)(N_{1-x}O_x)$ NW. a) High-resolution and b) reciprocal space analysis both reveal a WZ/ZB heterostructure associated with the stacking order of closed packed $\{001\}_{WZ}$ and $\{111\}_{ZB}$ planes along the wires $[001]_{WZ}$ growth direction.

ADVANCED
SCIENCE NEWS

www.advancedsciencenews.com

NANO · MICRO

small

www.small-journal.com

The WZ/ZB polytypism which is often observed in nanoscale III–V semiconductors is attributed to small differences in the energy landscape. Numerous reports exist about GaN thin films grown on various substrates[66–69] and GaN WZ nanowires[70–73] in which small ZB domains introduce quantum-well like electronic transition states. Hence, the controlled design of the defect structure, growth orientation, and crystal dimensions of heterostructure NWs for purposive application is investigated thoroughly by studying the growth kinetics[64,65] and the influence of the substrate and metal catalyst.

For example, the ability to control the direction of growth has been demonstrated by the choice of the substrate or metal catalyst in VLS or metal-organic chemical vapor deposition (MOCVD) growth environments. For example, Kuykendall used lattice-matched substrates,[74] e.g., (100) LiAlO$_2$ surfaces to grow GaN nanowires along [1-10]$_{WZ}$ and (111) MgO to achieve [001]$_{WZ}$ directed growth. Further, Au or Ni terminated NWs reported by Kuykendall[75] predominantly show [210]$_{WZ}$ growth, whereas Fe as catalyst leads to the growth along [100]$_{WZ}$.

For the present example of oxynitride solid solution phase heterostructures (Ga$_{1-x}$Zn$_x$)(N$_{1-x}$O$_x$) with x = 0.12, TEM studies on NWs catalytically grown in a VLS process starting from Au particles described crystal growth along [100]$_{WZ}$[62] and intentionally tuning of the crystallographic facets from non-polar to semipolar and polar by controlling temperature and nitridation time.[76]

The structure examination of the present individual single crystal (Ga$_{1-x}$Zn$_x$)(N$_{1-x}$O$_x$) nanowires in this study revealed growth along the polar [001]$_{WZ}$ and mixed nonpolar [012]$_{WZ}$/[010]$_{WZ}$ crystallographic directions, featuring the formation of kinks. The crystal structure of a kinked NW is further discussed in **Figure 6**. The mechanisms of kink formation and change of growth directions are widely discussed in the literature and can be narrowed down to a perturbation of the trijunction vapor–

liquid–solid energies[77] for ZB as well as WZ systems. Hence, the intentional introduction of kinks and switch of the growth direction was reported to be achieved, e.g., by keeping control of the droplet composition,[78] the temperature regime[79] and the growth atmosphere, by regulating the gas pressure or the supply of reactants.[80,81]

In the highly reactive growth environment inside GaN/ZnO microtubes, all those factors possibly take part in multiple kinking events of solid solution NWs. With respect to the nanostructure, the formation of kinks is often accompanied by crystal defects such as stacking faults or twin planes, especially in WZ/ZB heterostructures.[82,83] The kinked NW presented in Figure 6 possesses a large number of stacking faults/twins on the {001}/{111} planes and changes its growth direction from [010]$_{WZ}$ to [012]$_{WZ}$ and back to [010]$_{WZ}$ (red box). We highlight that the crystallographic orientation of (001)$_{WZ}$ planes does not change with respect to the electron beam after the kink but the lamellar stacking faults/twins run down the length of the wire to end at the metal catalyst (green box, Figure 6b).

In fact, the initial control of the supersaturated starting catalyst Au$_{1-x}$Ga$_x$ has been proven to be an essentially valuable parameter for the growth of unidirectional and pure phase GaAs NWs with minimal defect concentration,[84] hence stable growth conditions could be achieved for operating with a physically stable droplet.[58] Furthermore, the volume of the initial Au droplets does not only determine the NW diameter but also the Ga concentration in the supersaturated droplets differentiating in low-melting-point (AuGa, Au$_2$Ga, and Au$_7$Ga$_3$) and high-melting-point (Au$_7$Ga$_2$) catalytic alloys of the binary AuGa system.[61]

In this study, the uncontrolled formation of Au$_{1-x}$Ga$_x$ binary alloys according to the reaction scheme is supported by the nanoanalytics (see the elemental distribution maps of Au and Ga provided in Figure 4).
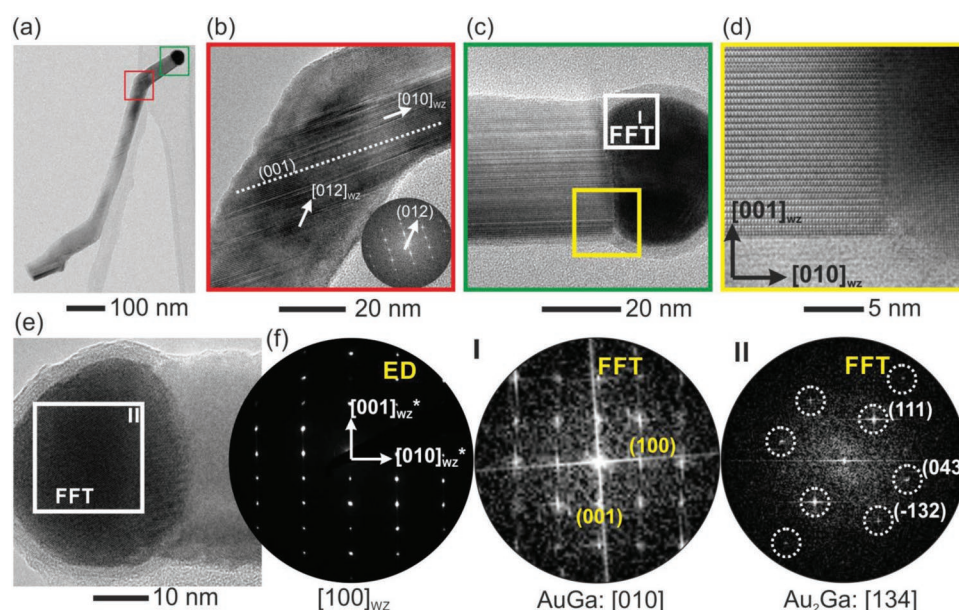

Figure 6. a) Overview image of a kinked NW and b) HRTEM micrograph of the kink region. c–e) HRTEM micrographs showing representative NWs with Au$_{1-x}$Ga$_x$ catalyst. d) Magnified image shoing the [001]_WZ lattice planes perpendicular to the [010]_WZ growth direction. f) Reciprocal space analysis via electron diffraction from the solid solution NW and FFT from the white framed regions on the Au$_{1-x}$Ga$_x$ catalyst crystals showing the formation of different AuGa -phases.
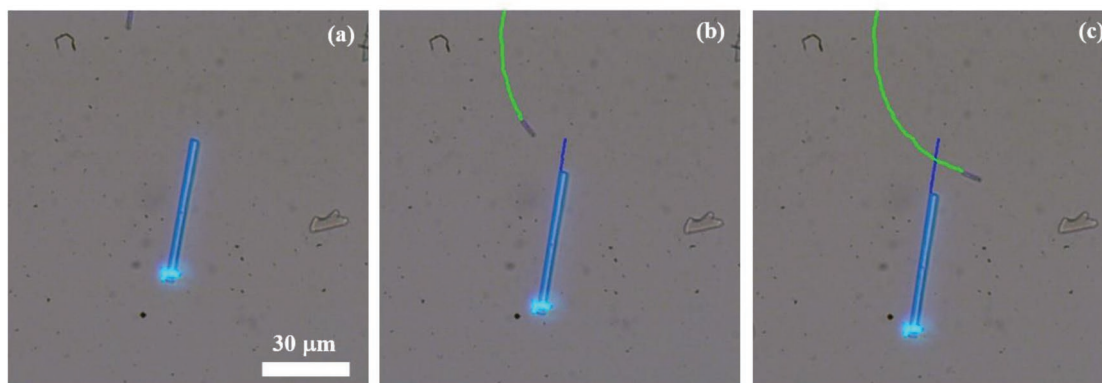
Figure 7. Optical image and corresponding tracking of two microtubes differing essentially in sizes. Motion under UV illumination: a) $t = 0$ s, b) after $t = 5$ s and c) after $t = 9$ s of irradiation. The small microtube is more than four times faster than the big one (5.5 µm s^{-1} compared to 1.4 µm s^{-1}). A 50 W UV power source was used.

Accordingly, the structural characterization via FFTs of HRTEM micrographs illustrated in Figure 6c confirms the existence of the stoichiometric orthorhombic phase AuGa[61] (Figure 6c.I) and the orthorhombic intermetallic γ-phase Au$_7$Ga$_3$ (Figure 6c.II), whose structure has been described by Puselj and Schubert in approximation to the Au$_2$Ga phase.[85] Unfortunately, the direct quantification of the chemical composition of individual catalysts has been restricted by amorphous residues of GaO$_x$ species forming a shell around the alloy observable in Figures 4 and 6b.

2.2. Light-Driven Micromotors

The light-driven motion characteristics of the functionalized nanoarchitectured GaN/ZnO microtubes are demonstrated in aqueous solutions of hydrogen peroxide.

Optical microscopy was utilized to follow two GaN/ZnO microtube-engines operating under UV irradiation (**Figure 7**) and their trajectories were recorded over 9 s (see Movie S2 in the Supporting Information). The investigated microtubes can easily be distinguished by their dimensions, the length and diameter of the larger (smaller) tube are 32 µm (4.6 µm) and 2 µm (0.9 µm), respectively. In order to illustrate the path of the microtubes under UV irradiation, the video files were processed using the ImageJ software. According to the acquired data, the average velocity of the small microtube was ≈5.5 µm s^{-1} while for the larger microtube it was 1.4 µm s^{-1}. The slower velocity of the larger microtube could be assigned to its higher surface area, which results in stronger drag forces in the liquid. Another interesting feature was the blue fluorescence exhibited by the GaN/ZnO microtubes under UV light, which is associated with the presence of a thin ZnO layer on the inner surface of the tube. The UV light-driven motion dynamics can be controlled by the on–off capability of the micromotors. Movie S3 (Supporting Information) shows the abrupt stop of the microtube motion by switching off the UV light accompanied by quenching of the fluorescence. In turn, the motion continues at a steady pace once the UV light was switched on again.

The GaN/ZnO microtubes prepared without gold dots (and thus without the growth of (Ga$_{1-x}$Zn$_x$)(N$_{1-x}$O$_x$) NWs on the inner surface) do not exhibit light-driven motion in hydrogen peroxide. This control experiment confirms that the presence of metal-dot-terminated NWs inside the GaN/ZnO microtubes plays a major role in creating a strong driving force resulting in the steady motion based on photocatalysis.

The most common propulsion mechanisms of tubular micromotors in hydrogen peroxide are based on bubble formation[36] and diffusiophoresis. Since bubble propulsion is inherent to bigger particles, the dominating mechanism of nanoarchitectured ZnO/GaN micromotor motion can be attributed to diffusiophoresis, which seems to occur mainly at the electrolyte interface with the thin layer of ZnO,[86] in our case decorated by metal-terminated heterogeneous NWs. Until now, ZnO micromotors were considered less applicable, due to the low stability of the material in an aqueous medium, however, the material has a high photocatalytic activity, which makes it promising for environmental applications. In our configuration, the GaN microtubes guarantee high chemical stability of the inner nanometer-thin layer of ZnO, which together with the AuGa-alloy nanodots and heterogeneous NWs accelerate the micromotors via diffusiophoresis generated by the photodegradation of hydrogen peroxide under UV light.

3. Conclusion

Novel hybrid nanoarchitectured GaN/ZnO microtubes with an outer hydrophobic GaN surface and an inner hydrophilic surface of chemically stabilized ZnO decorated by solid solution (Ga$_{1-x}$Zn$_x$)(N$_{1-x}$O$_x$) NWs, which are terminated by co-catalyst AuGa-alloy nanodots have been developed and characterized extensively by transmission electron microscopy. Our experiments show intense photocatalytic reactions under UV light excitation in the presence of hydrogen peroxide exclusively for decorated microtubes. It has been demonstrated that two microtubes with the lengths of 32 µm and 4.6 µm, and diameters of 2 µm and 0.9 µm, exhibit average velocities of UV-light-driven motion of 1.4 µm s^{-1} and 5.5 µm s^{-1} with switchable on–off capability. The obtained results are in line with literature data arguing that the process of diffusiophoresis could be responsible for the UV-light driven motion of microtubes.

ADVANCED
SCIENCE NEWS
www.advancedsciencenews.com

NANO · MICRO
small
www.small-journal.com

The GaN/ZnO nanoarchitectured microtubes prove to be very promising for the development of fluorescent micromotors, the fluorescence being generated by the nanoscale-thin ZnO film exhibiting high chemical stability at the interface with GaN. The developed micromotors seem very promising for sensing applications, e.g., by monitoring the fluorescence quenching in the presence of a certain analyte/environment or environmental cleaning by the degradation of organic pollutants by photocatalytic reactions. The presented synthesis approach can be adapted to various morphologies of ZnO microstructures and different metal catalysts, expanding the field of future in-depth studies of architecture-dependent photocatalytic properties with respect to template-based design engineering for device implementation.

4. Experimental Section

Growth Mechanism: In this work, the used hedgehog-like ZnO structures (microneedles) were obtained by a modified flame transport synthesis (FTS) previously reported by Mishra et al.[55] Similar to the FTS process, polyvinyl butane (PVB) and ethanol (purchased from Carl Roth ≥99.8% p.a.) were mixed at a ratio of (2:1). To obtain a bubble-free solution, the mixture was allowed to rest for 14 h. The primary precursor, Zn wire (purchased from Alfa Aesar GmbH & Co KG, Germany) was weighed and dipped into the PVB/ethanol solution. This coated Zn wire was set in a closed ceramic crucible and placed in a muffle furnace, preheated to 500 °C. It was then heated to 950 °C for 20 min. The furnace was cooled to 500 °C before removing the crucible. Once the crucible reached room temperature (20 °C) the ZnO hedgehogs were collected for further experiments. A gold thin film of a few nanometers was deposited on the ZnO microneedles in a Cressington 108 Sputter Coater machine. Subsequently, the samples were exposed to thermal treatment at 300 °C for 1 h in the atmosphere. The thermal treatment leads to the transformation of a continuous Au film into uniformly distributed Au dots. After this decoration step, the ZnO microneedles were used as sacrificial templates for the growth of GaN in an HVPE system. As previously reported,[31] the system is equipped with a four-temperature-zone-heated horizontal reactor, where metallic gallium, ammonia gas and hydrogen chloride gas were used as source materials while hydrogen was used as the carrier gas. The GaCl was formed during the reaction between HCl and Ga in the source zone where the temperature was kept at 850 °C. The formed GaCl was then transported by H_2 gas in the reaction zone where interaction with NH_3 gas at 600 °C for 10 min initiated the nucleation of GaN on the surface of the ZnO microneedles. Then, the temperature was increased up to 850 °C for 10 min to grow a thin GaN layer. In the process of GaN growth, the HCl, NH_3, and H_2 flow rates were equal to 15 500, and 3600 sml min^{-1} (standard mililiters per minute), respectively.

Motion Analysis: To study the motion of the GaN/ZnO microtubes, 10 wt% of H_2O_2 aqueous solution with 1.3 wt% of sodium dodecyl sulfate (SDS) was used. The microtubes were placed in a confined space (cell), specially designed to avoid fluxes associated with solvent evaporation and to provide stable conditions for a reliable analysis of their motion and other related phenomena.

The videos and images of the samples were taken using a Zeiss microscope setup, Zeiss Axio Scope.A1, equipped with a camera, and an EC Plan -Neofluar 40× /0.75 lens. The GaN/ZnO microtubes were irradiated using a 50 W UV light source from the previously mentioned optical microscope.

Structural Characterization: The structural characterization of the GaN/ZnO nanoarchitectured microtubes was performed using the analytical capabilities of transmission electron microscopy. The microscopes used during the study involved a Tecnai F30 STwin (300 kV, field-emission gun, spherical aberration constant C_s = 1.2 mm) and a Philipps CM 30 ST (300 kV, C_s = 1.15 mm). High-resolution TEM and electron diffraction in combination with precession electron diffraction and fast Fourier transform analysis were used to study the crystal structure of the GaN/ZnO microtubes and AuGa-terminated wires. The compositional analysis of the GaN/ZnO microtubes was carried out using energy-dispersive X-ray spectroscopy in combination with TEM and scanning TEM with a high-angle annular dark field detector for imaging. A 3D model of the morphology was computed by STEM tomography using a special single tilt tomography holder to allow for sample tilts in the range of −70° to + 70° minimizing the distortions from the missing wedge. A STEM tomography linear tilt series with a step size of 1° was recorded to compute the reconstruction model, which is based on an algorithm called filtered back projection real space reconstruction.[87,88] The isosurfaces of the volume reconstruction were color-coded to differentiate between the microtubes and wires.

Supporting Information

Supporting Information is available from the Wiley Online Library or from the author.

Conflict of Interest

The authors declare no conflict of interest.

[1] F. Fresno, R. Portela, S. Suárez, J. M. Coronado, *J. Mater. Chem. A* **2014**, *2*, 2863.
[2] L. Yu, H. B. Wu, X. W. D. Lou, *Acc. Chem. Res.* **2017**, *50*, 293.
[3] A. Huczko, *Appl. Phys. A: Mater. Sci. Process.* **2000**, *70*, 365.
[4] A.-H. Lu, F. Schüth, *Adv. Mater.* **2006**, *18*, 1793.
[5] R. Ryoo, S. H. Joo, S. Jun, *J. Phys. Chem. B* **1999**, *103*, 7743.
[6] T. Kyotani, T. Nagai, S. Inoue, A. Tomita, *Chem. Mater.* **1997**, *9*, 609.
[7] F. Schüth, *Angew. Chem.* **2003**, *115*, 3730.
[8] Q. Wei, Y. Fu, G. Zhang, D. Yang, G. Meng, S. Sun, *Nano Energy* **2019**, *55*, 234.
[9] Z.-X. Cai, Z.-L. Wang, J. Kim, Y. Yamauchi, *Adv. Mater.* **2019**, *31*, 1804903.
[10] H.-H. Li, S.-H. Yu, *Adv. Mater.* **2019**, *31*, 1803503.
[11] Y. K. Mishra, R. Adelung, *Mater. Today* **2018**, *21*, 631.

[12] I. Hölken, G. Neubüser, V. Postica, L. Bumke, O. Lupan, M. Baum, Y. K. Mishra, L. Kienle, R. Adelung, *ACS Appl. Mater. Interfaces* **2016**, *8*, 20491.

[13] M. Mecklenburg, A. Schuchardt, Y. K. Mishra, S. Kaps, R. Adelung, A. Lotnyk, L. Kienle, K. Schulte, *Adv. Mater.* **2012**, *24*, 3486.

[14] F. Schütt, S. Signetti, H. Krüger, S. Röder, D. Smazna, S. Kaps, S. N. Gorb, Y. K. Mishra, N. M. Pugno, R. Adelung, *Nat. Commun.* **2017**, *8*, 1215.

[15] I. Tiginyanu, T. Braniste, D. Smazna, M. Deng, F. Schütt, A. Schuchardt, M. A. Stevens-Kalceff, S. Raevschi, U. Schürmann, L. Kienle, N. M. Pugno, Y. K. Mishra, R. Adelung, *Nano Energy* **2019**, *56*, 759.

[16] J. Goldberger, R. He, Y. Zhang, S. Lee, H. Yan, H.-J. Choi, P. Yang, *Nature* **2003**, *422*, 599.

[17] T. Detchprohm, K. Hiramatsu, H. Amano, I. Akasaki, *Appl. Phys. Lett.* **1992**, *61*, 2688.

[18] H. J. Fan, F. Fleischer, W. Lee, K. Nielsch, R. Scholz, M. Zacharias, U. Gösele, A. Dadgar, A. Krost, *Superlattices Microstruct.* **2004**, *36*, 95.

[19] C.-H. Chen, S.-J. Chang, S.-P. Chang, M.-J. Li, I.-C. Chen, T.-J. Hsueh, C.-L. Hsu, *Chem. Phys. Lett.* **2009**, *476*, 69.

[20] M.-C. Jeong, B.-Y. Oh, M.-H. Ham, S.-W. Lee, J.-M. Myoung, *Small* **2007**, *3*, 568.

[21] H. Chen, Q. Zhao, X. Du, *Micromachines* **2018**, *9*, 41.

[22] M. Enachi, M. Guix, V. Postolache, V. Ciobanu, V. M. Fomin, O. G. Schmidt, I. Tiginyanu, *Small* **2016**, *12*, 5497.

[23] R. Dong, C. Wang, Q. Wang, A. Pei, X. She, Y. Zhang, Y. Cai, *Nanoscale* **2017**, *9*, 15027.

[24] M. Asif Khan, J. N. Kuznia, J. M. Van Hove, D. T. Olson, S. Krishnankutty, R. M. Kolbas, *Appl. Phys. Lett.* **1991**, *58*, 526.

[25] T. Kawashima, H. Yoshikawa, S. Adachi, S. Fuke, K. Ohtsuka, *J. Appl. Phys.* **1997**, *82*, 3528.

[26] H. S. Jung, Y. J. Hong, Y. Li, J. Cho, Y.-J. Kim, G.-C. Yi, *ACS Nano* **2008**, *2*, 637.

[27] Y. K. Lim, E. W. Keong Koh, Y.-W. Zhang, H. Pan, *J. Power Sources* **2013**, *232*, 323.

[28] B. Ren, X. Zhang, M. Zhao, X. Wang, J. Ye, D. Wang, *AIP Adv.* **2018**, *8*, 015206.

[29] A. Wu, J. Li, B. Liu, W. Yang, Y. Jiang, L. Liu, X. Zhang, C. Xiong, X. Jiang, *Dalton Trans.* **2017**, *46*, 2643.

[30] J. P. Sundararajan, P. Bakharev, I. Niraula, B. A. Fouetio Kengne, Q. MacPherson, M. Sargent, B. Hare, D. N. McIlroy, *Nano Lett.* **2012**, *12*, 5181.

[31] F. Qin, N. Chang, C. Xu, Q. Zhu, M. Wei, Z. Zhu, F. Chen, J. Lu, *RSC Adv.* **2017**, *7*, 15071.

[32] M. Medina-Sánchez, O. G. Schmidt, *Nature* **2017**, *545*, 406.

[33] J. Li, I. Rozen, J. Wang, *ACS Nano* **2016**, *10*, 5619.

[34] W. F. Paxton, S. Sundararajan, T. E. Mallouk, A. Sen, *Angew. Chem., Int. Ed.* **2006**, *45*, 5420.

[35] W. F. Paxton, K. C. Kistler, C. C. Olmeda, A. Sen, S. K. St. Angelo, Y. Cao, T. E. Mallouk, P. E. Lammert, V. H. Crespi, *J. Am. Chem. Soc.* **2004**, *126*, 13424.

[36] A. A. Solovev, Y. Mei, E. B. Ureña, G. Huang, O. G. Schmidt, *Small* **2009**, *5*, 1688.

[37] J. R. Howse, R. A. L. Jones, A. J. Ryan, T. Gough, R. Vafabakhsh, R. Golestanian, *Phys. Rev. Lett.* **2007**, *99*, 048102.

[38] M. Su, V. P. Dravid, *Nano Lett.* **2005**, *5*, 2023.

[39] F. Mou, Y. Li, C. Chen, W. Li, Y. Yin, H. Ma, J. Guan, *Small* **2015**, *11*, 2564.

[40] R. Dong, Y. Cai, Y. Yang, W. Gao, B. Ren, *Acc. Chem. Res.* **2018**, *51*, 1940.

[41] I. Buttinoni, G. Volpe, F. Kümmel, G. Volpe, C. Bechinger, *J. Phys.: Condens. Matter* **2012**, *24*, 284129.

[42] L. Xu, F. Mou, H. Gong, M. Luo, J. Guan, *Chem. Soc. Rev.* **2017**, *46*, 6905.

[43] S. Sanchez, A. N. Ananth, V. M. Fomin, M. Viehrig, O. G. Schmidt, *J. Am. Chem. Soc.* **2011**, *133*, 14860.

[44] R. Dong, Q. Zhang, W. Gao, A. Pei, B. Ren, *ACS Nano* **2016**, *10*, 839.

[45] S. Jeon, S. Kim, S. Ha, S. Lee, E. Kim, S. Y. Kim, S. H. Park, J. H. Jeon, S. W. Kim, C. Moon, B. J. Nelson, J. Kim, S.-W. Yu, H. Choi, *Sci. Rob.* **2019**, *4*, eaav4317.

[46] B. E.-F. de Ávila, P. Angsantikul, J. Li, M. A. Lopez-Ramirez, D. E. Ramírez-Herrera, S. Thamphiwatana, C. Chen, J. Delezuk, R. Samakapiruk, V. Ramez, M. Obonyo, L. Zhang, J. Wang, *Nat. Commun.* **2017**, *8*, 272.

[47] M. Medina-Sánchez, L. Schwarz, A. K. Meyer, F. Hebenstreit, O. G. Schmidt, *Nano Lett.* **2016**, *16*, 555.

[48] S. Balasubramanian, D. Kagan, C.-M. Jack Hu, S. Campuzano, M. J. Lobo-Castañon, N. Lim, D. Y. Kang, M. Zimmerman, L. Zhang, J. Wang, *Angew. Chem., Int. Ed.* **2011**, *50*, 4161.

[49] J. Li, V. V. Singh, S. Sattayasamitsathit, J. Orozco, K. Kaufmann, R. Dong, W. Gao, B. Jurado-Sanchez, Y. Fedorak, J. Wang, *ACS Nano* **2014**, *8*, 11118.

[50] B. Jurado-Sánchez, J. Wang, *Environ. Sci.: Nano* **2018**, *5*, 1530.

[51] L. Wang, A. Kaeppler, D. Fischer, J. Simmchen, *ACS Appl. Mater. Interfaces* **2019**, *11*, 32937.

[52] S. K. Srivastava, M. Guix, O. G. Schmidt, *Nano Lett.* **2016**, *16*, 817.

[53] L. Soler, V. Magdanz, V. M. Fomin, S. Sanchez, O. G. Schmidt, *ACS Nano* **2013**, *7*, 9611.

[54] M. Guix, J. Orozco, M. García, W. Gao, S. Sattayasamitsathit, A. Merkoçi, A. Escarpa, J. Wang, *ACS Nano* **2012**, *6*, 4445.

[55] Y. K. Mishra, S. Kaps, A. Schuchardt, I. Paulowicz, X. Jin, D. Gedamu, S. Freitag, M. Claus, S. Wille, A. Kovalev, S. N. Gorb, R. Adelung, *Part. Part. Syst. Charact.* **2013**, *30*, 775.

[56] S. Bals, S. Van Aert, G. Van Tendeloo, *Curr. Opin. Solid State Mater. Sci.* **2013**, *17*, 107.

[57] P. A. Midgley, M. Weyland, *Ultramicroscopy* **2003**, *96*, 413.

[58] S. N. Mohammad, *Nano Lett.* **2008**, *8*, 1532.

[59] D. Elwell, M. M. Elwell, *Prog. Cryst. Growth Charact.* **1988**, *17*, 53.

[60] V. Gottschalch, G. Wagner, J. Bauer, H. Paetzelt, M. Shirnow, *J. Cryst. Growth* **2008**, *310*, 5123.

[61] C. J. Cooke, W. Hume-Rothery, *J. Less-Common Met.* **1966**, *10*, 42.

[62] W.-Q. Han, Y. Zhang, C.-Y. Nam, C. T. Black, E. E. Mendez, *Appl. Phys. Lett.* **2010**, *97*, 083108.

[63] P. A. Midgley, A. S. Eggeman, *IUCrJ* **2015**, *2*, 126.

[64] K. A. Dick, P. Caroff, J. Bolinsson, M. E. Messing, J. Johansson, K. Deppert, L. R. Wallenberg, L. Samuelson, *Semicond. Sci. Technol.* **2010**, *25*, 024009.

[65] P. Caroff, K. A. Dick, J. Johansson, M. E. Messing, K. Deppert, L. Samuelson, *Nat. Nanotechnol.* **2009**, *4*, 50.

[66] L. López-Conesa, J. A. Pérez-Omil, Ž. Gačević, E. Calleja, S. Estradé, F. Peiró, *Phys. Status Solidi A* **2018**, *215*, 1800218.

[67] A. Trampert, O. Brandt, K. H. Ploog, *Angew. Chem.* **1997**, *109*, 2202.

[68] T. Lei, K. F. Ludwig, T. D. Moustakas, *J. Appl. Phys.* **1993**, *74*, 4430.

[69] B. M. Shi, M. H. Xie, H. S. Wu, N. Wang, S. Y. Tong, *Appl. Phys. Lett.* **2006**, *89*, 151921.

[70] G. Jacopin, L. Rigutti, L. Largeau, F. Fortuna, F. Furtmayr, F. H. Julien, M. Eickhoff, M. Tchernycheva, *J. Appl. Phys.* **2011**, *110*, 064313.

[71] D. Tham, C.-Y. Nam, J. E. Fischer, *Adv. Funct. Mater.* **2006**, *16*, 1197.

[72] M. Heiss, S. Conesa-Boj, J. Ren, H.-H. Tseng, A. Gali, A. Rudolph, E. Uccelli, F. Peiró, J. R. Morante, D. Schuh, E. Reiger, E. Kaxiras, J. Arbiol, A. Fontcuberta i Morral, *Phys. Rev. B* **2011**, *83*, 045303.

[73] J. Arbiol, S. Estradé, J. D. Prades, A. Cirera, F. Furtmayr, C. Stark, Andreas Laufer, M. Stutzmann, M. Eickhoff, M. H. Gass, A. L. Bleloch, F. Peiró, J. R. Morante, *Nanotechnology* **2009**, *20*, 145704.

[74] T. Kuykendall, P. J. Pauzauskie, Y. Zhang, J. Goldberger, D. Sirbuly, J. Denlinger, P. Yang, *Nat. Mater.* **2004**, *3*, 524.

[75] T. Kuykendall, P. Pauzauskie, S. Lee, Y. Zhang, J. Goldberger, P. Yang, *Nano Lett.* **2003**, *3*, 1063.

[76] J. Li, B. Liu, W. Yang, Y. Cho, X. Zhang, B. Dierre, T. Sekiguchi, A. Wu, X. Jiang, *Nanoscale* **2016**, *8*, 3694.

[77] K. W. Schwarz, J. Tersoff, *Nano Lett.* **2011**, *11*, 316.

[78] J. Wang, S. R. Plissard, M. A. Verheijen, L.-F. Feiner, A. Cavalli, E. P. A. M. Bakkers, *Nano Lett.* **2013**, *13*, 3802.

[79] X. Yang, B. Zhou, C. Liu, Y. Sui, G. Xiao, Y. Wei, X. Wang, B. Zou, *Nano Res.* **2017**, *10*, 2311.

[80] I. R. Musin, M. A. Filler, *Nano Lett.* **2012**, *12*, 3363.

[81] B. Tian, P. Xie, T. J. Kempa, D. C. Bell, C. M. Lieber, *Nat. Nanotechnol.* **2009**, *4*, 824.

[82] F. M. Davidson, D. C. Lee, D. D. Fanfair, B. A. Korgel, *J. Phys. Chem. C* **2007**, *111*, 2929.

[83] R. E. Algra, M. A. Verheijen, M. T. Borgström, L.-F. Feiner, G. Immink, W. J. P. van Enckevort, E. Vlieg, E. P. A. M. Bakkers, *Nature* **2008**, *456*, 369.

[84] N. Han, F. Wang, J. J. Hou, S. Yip, H. Lin, M. Fang, F. Xiu, X. Shi, T. Hung, J. C. Ho, *Cryst. Growth Des.* **2012**, *12*, 6243.

[85] M. Pušelj, K. Schubert, *J. Less-Common Met.* **1974**, *38*, 83.

[86] A. M. Pourrahimi, K. Villa, Y. Ying, Z. Sofer, M. Pumera, *ACS Appl. Mater. Interfaces* **2018**, *10*, 42688.

[87] P. A. Penczek, in *Methods in Enzymology* (Ed.: G. J. Jensen), Academic Press, San Diego, CA **2010**, pp. 1–33.

[88] D. Wolf, A. Lubk, H. Lichte, *Ultramicroscopy* **2014**, *136*, 15.